Accelerated Diffusion Kinetics in ZnTe/CoTe$_2$ Heterojunctions for High Rate Potassium Storage

Chaofeng Zhang,* Hao Li, Xiaohui Zeng, Shibo Xi, Rui Wang, Longhai Zhang, Gemeng Liang, Kenneth Davey, Yuping Liu, Lin Zhang, Shilin Zhang,* and Zaiping Guo*

Potassium-ion batteries hold practical potential for large-scale energy storage owing to their appealing cell voltage and cost-effective features. The development of anode materials with high rate capability and satisfactory cycle lifespan, however, is one of the key elements for exploiting this electrochemical energy storage system at practical levels. Here, a template-assisted strategy is reported for acquiring a bimetallic telluride heterostructure which is supported on N-doped carbon shell (ZnTe/CoTe$_2$@NC) that promotes diffusion of K$^+$ ions for rapid charge transfer. It is shown that in telluride heterojunctions, electron-rich Te sites and built-in electric fields contributed by electron transfer from ZnTe to CoTe$_2$ concomitantly provide abundant cation adsorption sites and facilitate interfacial electron transport during potassiation/depotassiation. The relatively fine ZnTe/CoTe$_2$ nanoparticles imparted by the heterojunction result in high structural stability, together with a highly reversible capacity up to 5000 cycles at 5 A g^{-1}. Moreover, using judiciously combined experiment and theoretical computation, it is demonstrated that the energy barrier for K$^+$ diffusion in telluride heterojunctions is significantly lower than that in individual counterparts. This quantitative design for fast and durable charge transfer in telluride heterostructures can be of immediate benefit for the rational design of batteries for low-cost energy storage and conversion.

1. Introduction

Potassium-ion batteries (PIBs) hold practical potential for large-scale electrical energy storage because of the advantages in natural abundance of potassium, comparatively low cost, and attractive redox potential of K/K$^+$ (−2.93 V for K/K$^+$ vs SHE).[1–4] Due to the significantly greater ionic radius of K$^+$ ions of 1.40 Å compared with that for Li$^+$ of 0.76 Å, however, the insertion of K$^+$ into electrode materials is sluggish, the current PIBs are still unsatisfactory to meet the requirement of high energy density and cycle lifespan.[5–7] Especially for the anode, carbonaceous materials have been widely studied while showing a relatively low capacity so far.[8,9] Significant research has looked to adapt alloys and metal oxides with improved capacity to PIBs based on existing lithium-ion battery technology but such materials tend to undergo extra volume expansion during potassiation/de-potassiation with poor cycling stability, especially at a high

C. Zhang, H. Li, R. Wang, L. Zhang
Institutes of Physical Science and Information Technology
Leibniz Joint Research Center of Materials Sciences
Engineering Laboratory of High-Performance Waterborne
Polymer Materials of Anhui Province
Anhui Graphene Engineering Laboratory
Key Laboratory of Structure and Functional Regulation
of Hybrid Material (Ministry of Education)
Anhui University
Hefei 230601, P. R. China
E-mail: cfz@ahu.edu.cn

The ORCID identification number(s) for the author(s) of this article can be found under https://doi.org/10.1002/aenm.202202577.

X. Zeng
Institute for Superconducting and Electronic Materials (ISEM)
Australian Institute for Innovative Materials (AIIM)
University of Wollongong
Wollongong, NSW 2522, Australia

S. Xi
Institute of Chemical and Engineering Sciences A*STAR
Singapore 627833, Singapore

G. Liang, K. Davey, S. Zhang, Z. Guo
School of Chemical Engineering & Advanced Materials
The University of Adelaide
Adelaide 5005, Australia
E-mail: Shilin.zhang01@adelaide.edu.au;
zaiping.guo@adelaide.edu.au

Y. Liu, L. Zhang
Institute for Solid State Physics
Laboratory of Nano and Quantum Engineering (LNQE)
Leibniz University Hannover
Appelstrasse 2, 30167 Hannover, Germany

rate.[10,11] There is a need therefore to produce new anode materials with boosted rate capacity and stable structures via rational design and controllable synthesis.

Materials suitable for high rate capability are those with rapid potassium-ion transfer kinetics that can be used practically as building blocks. Amongst these, transition metal tellurides (TMTs) are of particular research interest because of distinctive ionic transfer kinetics, safe potential plateau, and multiple electrochemical reactions, i.e., conversion and alloying.[12,13] TMTs present greater lattice parameters and have better electrical conductivity than sulfides, and selenides because of the larger atomic number and lower electronegativity of Te, with the expectation of boosted kinetics.[14] Additionally, TMTs have a higher density than corresponding sulfides and selenides, and therefore contribute to a greater volumetric capacity.[15] Importantly, TMTs are typical layered materials that exhibit highly significant interlayer space that favors diffusion of the rapid potassium ions in the electrode to give good electrode wettability and ion diffusion kinetics. However, tellurides have several limitations, including an intrinsic semiconductor nature, possible structural variation/pulverization, and an unclear potassium storage mechanism(s).

In terms of rational structure design, heterostructures formed by combination of nanocrystals with differing bandgap values is a favorable architecture that could help circumvent the issues in TMTs anode of PIBs.[16] In particular, the heterostructures can i) afford a higher electrochemical storage activity than that of their counterparts due to the variety of synergic effects that heterostructure materials might hold; ii) enhance the electronic conductivity because of the refined energy band structures with smaller bandgaps; iii) accelerate the ionic transfer kinetics with lower diffusion barrier due to the introduction of the internal electric field. iv) accommodate volume expansion and maintain structural stability owing to the strong interactions such as chemical bonds and electrostatic force.[17,18] Unfortunately, the research of heterostructural TMTs on PIBs is still at an early stage, with the underlying electrochemical mechanism unclear, and only a few candidates could present reasonable high rate capability, despite the cycling performance being far from practical application.

Bearing the abovementioned points in mind, herein, we report a template-assisted strategy to produce ZnTe/CoTe$_2$ heterostructure covered by N-doped carbon that is derived from Zn/Co-ZIF-67 template. Intentional substitution of Co with Zn in ZIF-67 affords a retarded rate of nucleation and leads to ZnTe/CoTe$_2$ heterostructure of relatively small size. Combining the desired features of promoted charge transfer kinetics and confined structural variation, the ZnTe/CoTe$_2$ heterostructure exhibits a highly significant rate capability and ultra-long cycle life (165.2 mAh g^{-1} at 5 A g^{-1} after 5000 cycles) as an anode for PIBs. We demonstrate a facile synthesis that permits practical tuning of the heterostructure for ready uptake of potassium ions, and which is generalizable for ions with a larger radius. We also confirm the morphology change and mechanism for potassium storage via combined findings from ex situ material characterizations, electrochemical technologies, in situ X-ray diffraction (XRD), and theoretical computations. Our new findings will be of immediate benefit for the design of low-cost PIBs for large-scale energy storage and conversion.

2. Results and Discussion

The synthesis for ZnTe/CoTe$_2$ heterostructure is shown schematically in **Figure 1**a. Zn/Co-ZIF-67 is obtained by selectively adding a mix of both metal salts Zn^{2+} and Co^{2+} combined with the ligand solution at room temperature (Methods in supporting information). The surface of Zn/Co-ZIF-67 is covered by a polydopamine (PDA) layer to obtain the Zn/Co-ZIF-67@PDA precursor, which is thermally treated with tellurium powder to obtain the ZnTe/CoTe$_2$@N-doped carbon heterostructure. Field-emission scanning electron microscopy (SEM) images in Figure 1b (Figures S1 and S2, Supporting Information) showed that ZIF-8, ZIF-67, and Zn/Co-ZIF-67 templates exhibit well-defined uniform metal organic framework dodecahedral structures with smooth surfaces. The SEM images in Figure 1c,d showed that the size and polyhedral shapes of Zn/Co-ZIF-67@PDA precursor and ZnTe/CoTe$_2$@NC were maintained following, respectively, PDA coating and thermal treatment, that was similar to the pristine Zn/Co-ZIF-67 template. The polyhedral size of ZnTe/CoTe$_2$@NC heterostructure was computed to be ≈238.9 nm (Figure S3, Supporting Information), a value close to that for pure Zn/Co-ZIF-67@PDA precursor. The surface of ZnTe/CoTe$_2$@NC polyhedra was apparently rougher following telluridation. Transmission electron microscopy (TEM, Figure 1e, and Figure S4) confirmed that a number of fine nanoparticles with an average diameter of 22.0 nm, are embedded regularly within the 3D, inter-connected, porous carbon framework, especially at the edge of the Zn/Co-ZIF-67@NC polyhedron.

The thickness of the N-doped carbonaceous wall was less than 10 nm (Figure 1f). It was observed that the nanoparticles in the polyhedron did not exhibit growth in the same direction, abundant edges rather than the basal plane were therefore exposed on the surface of the shell. These provide abundant electrode/electrolyte contact surface resulting in boosted charge transfer.[19,20] Additionally, as is highlighted in the magnified TEM image (Figure 1f) numerous pores in the carbon matrix introduce convenient diffusion paths for ionic transport.[20] The high resolution TEM image of Figure 1g highlights well-defined heterojunction interfaces where lattice fringes with a width of 0.194 nm agrees with the (200) facet of CoTe$_2$, and the width, 0.215 nm agrees with the (220) facet of ZnTe (Figure S5). As is highlighted in Figure 1h, N, Te, Zn, and Co elements are homogeneously distributed without apparent particle aggregation. As was evidenced in the EDX spectrum data there was ~42.0 wt.% carbon in the ZnTe/CoTe$_2$@NC sample (Figure S6, Supporting Information). In contrast, however, following processing with similar telluridation both ZnTe@NC (Figure S7, Supporting Information) and CoTe$_2$@NC (Figure S8, Supporting Information) exhibited apparent shrinking and collapsing on the polyhedra surfaces, together with significantly greater polyhedral size (Figure S3, Supporting Information) when compared with ZIF-8@PDA and ZIF-67@PDA precursors. This finding is attributed to the disparity in the rate of nucleation and growth with Zn/Co-ZIF-67, Zn-ZIF-8, and Co-ZIF-67. It is established that nucleation of ZIF-8 dominates crystal formation, whereas growth governs with ZIF-67 to result in meaningfully larger crystals throughout reaction–diffusion.[21,22] Additionally, measured
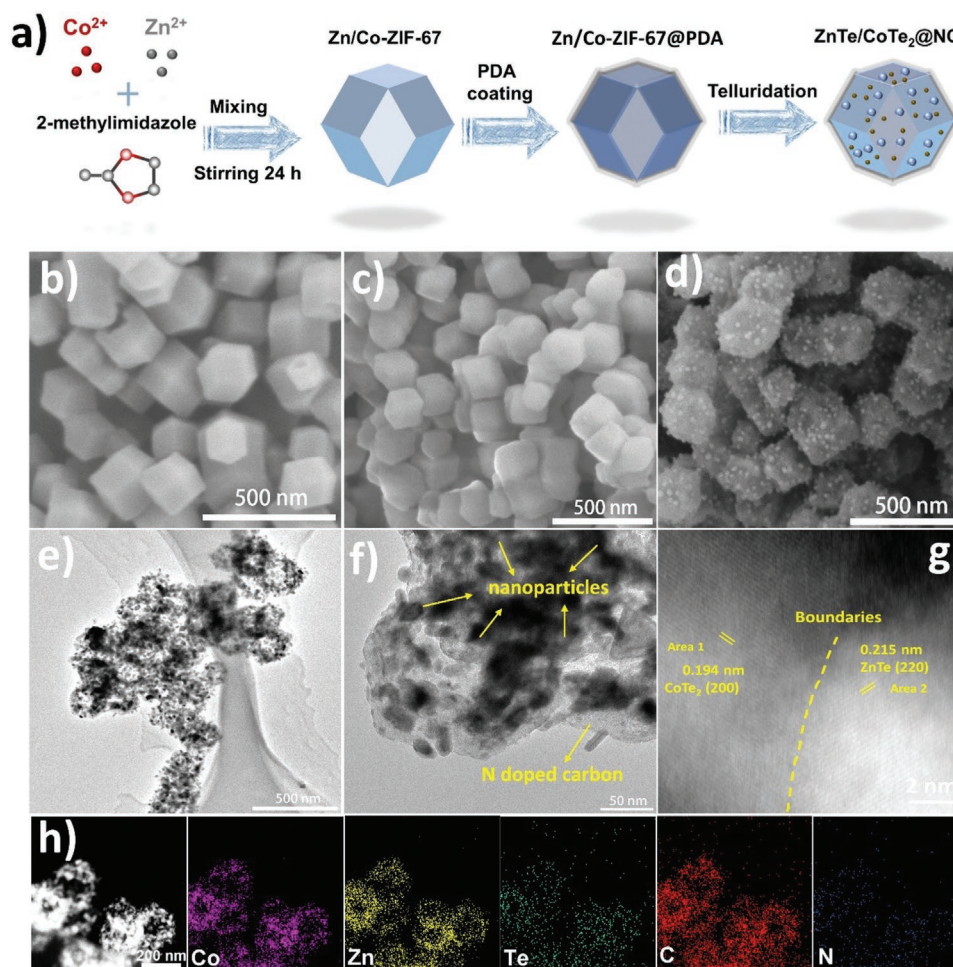
Figure 1. Morphology characterization. a) Schematic for preparation of ZnTe/CoTe$_2$@NC. b–d) Representative SEM images of Zn/Co-ZIF-67, Zn/Co-ZIF-67@PDA and ZnTe/CoTe$_2$@NC. e–f) TEM images of ZnTe/CoTe$_2$@NC. g) HAADF-STEM image of ZnTe/CoTe$_2$@NC, and h) STEM-EDS element mapping.

particle size for heterostructural ZnTe/CoTe$_2$@NC crystals were consistently smaller than for CoTe$_2$ in CoTe$_2$@NC of 35.0 nm and ZnTe in ZnTe@NC of 32.5 nm (Figure S4, Supporting Information). This finding is attributed to the different growth mechanisms amongst Zn/Co-ZIF-67, Zn-ZIF-8, and Co-ZIF-67. With the addition of Zn^{2+} species to Co-ZIF-67, the Zn^{2+} ions act as "impurities" in crystal nucleation and growth in which zinc delays the kinetics of nucleation and leads to doped particles of relatively smaller size.[21]

The crystalline phase and composition of the as-synthesized materials were evidenced by findings from powder XRD as highlighted in **Figure 2**a. As is shown in the XRD pattern for ZnTe/CoTe$_2$@NC representative peaks located at 25.3, 41.8 and 49.5° can be readily attributed to the (111), (220), and (311) facets of cubic ZnTe (PDF: # 65–5730), whilst the peaks located at about 28.5, 31.9, 33.0, 43.7, and 58.5° can be readily, respectively, attributed to the (110), (111), (012), (121), and (212) planes of the orthorhombic CoTe$_2$ (PDF: #74-0245). This finding confirms the formation of ZnTe/CoTe$_2$ heterostructure in ZnTe/CoTe$_2$@NC, and supports that from HRTEM observations of Figure 1g (and Figure S7d–S8d, Supporting Information). No specific peaks can

be attributed to the carbon species because of a peak overlap at around 25° in ZnTe/CoTe$_2$@NC. However, the carbon species can be assessed by the Raman shift for the products. Figure 2b highlights two distinct peaks at 1330 and 1571 cm^{-1}, which are, respectively, the vibration of the D band (disordered or defect carbon) and G band (graphitic sp^{2-} carbon). The intensity ratio of the D and G band, I_D/I_G, is, respectively, 0.87, 0.89, and 1.01 for CoTe$_2$@NC, ZnTe@NC, and ZnTe/CoTe$_2$@NC. This result demonstrates that the introduction of Zn species and/or smaller particles in ZnTe/CoTe$_2$@NC promotes the formation of more disordered graphitic carbon. Additionally, a typical type IV nitrogen adsorption/desorption isotherm with an H1 hysteresis loop was observed for all three samples. This is indicative of mesoporous structure (Figure S9, Supporting Information). ZnTe/CoTe$_2$@NC, CoTe$_2$@NC, and ZnTe@NC show specific surface-area (SSA) based on Brunauer–Emmett–Teller method of, respectively, around 131.7, 129.2, and 86.4 m^2 g^{-1}. The greatest value of SSA for ZnTe/CoTe$_2$@NC is attributed to large pore volume.

Figure 2c–e presents the chemical composition of samples determined using X-ray photoelectron spectroscopy (XPS). The
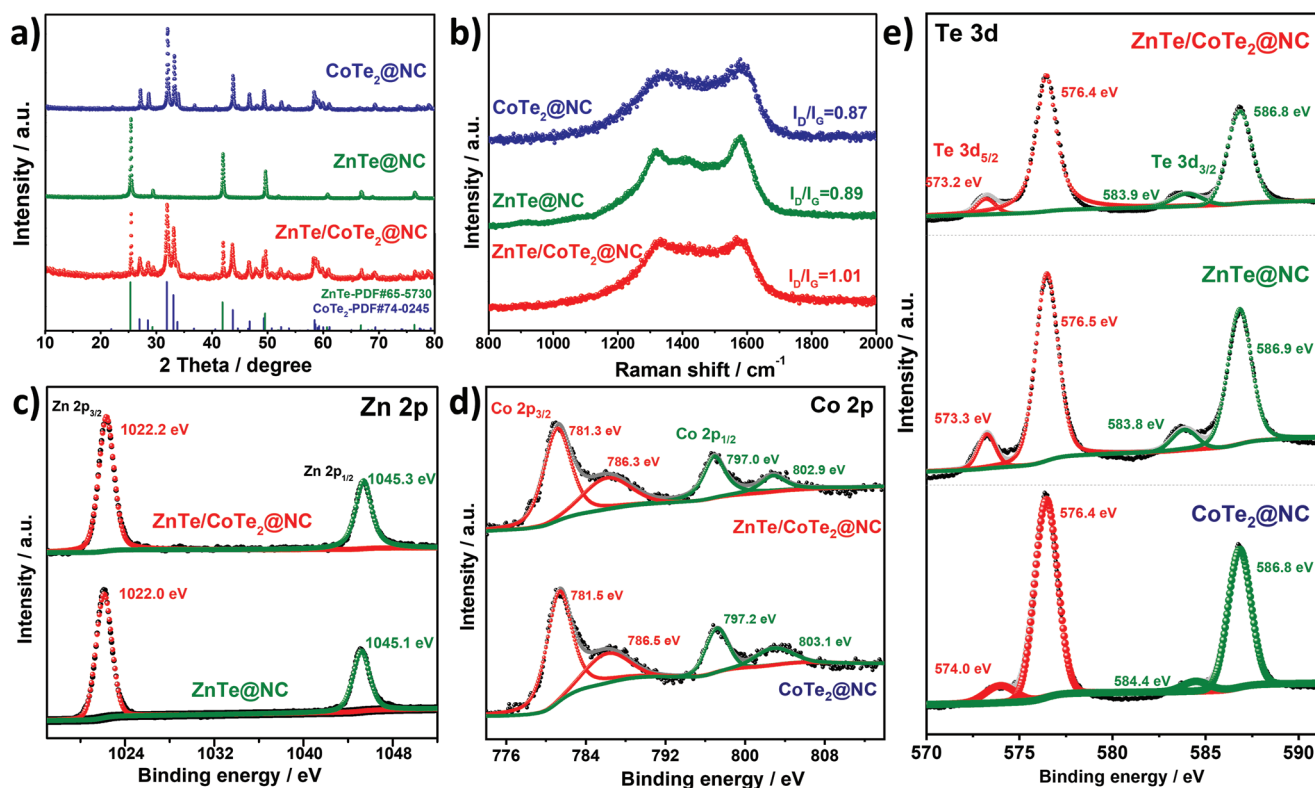
Figure 2. Characterization of ZnTe@NC, CoTe$_2$@NC and ZnTe/CoTe$_2$@NC. a) XRD pattern. b) Raman spectra. c) XPS spectra for Zn 2p. d–e) XPS spectra for Co 2p and Te 3d.

Zn 2p signal in the ZnTe/CoTe$_2$@NC heterostructure is seen to be divided into two peaks at 1022.2 and 1045.3 eV, toward high binding energy compared with that in ZnTe@NC. This finding confirms a decrease in the electronic density of Zn^{2+} ions. Whilst driven by the built-in electric field originating from the heterojunction, the negative signal shifts for Co 2p$_{3/2}$ from 781.5 to 781.3 eV, and 2p$_{1/2}$ from 787.2 to 787.0 eV, confirm electrons transferred from ZnTe to CoTe$_2$ in the ZnTe/CoTe$_2$@NC heterostructure.[23,24] The redistribution of interfacial charge underscores the electronic interaction between ZnTe and CoTe$_2$ domains.[25] The peaks located at 573.2 and 583.9 eV in the Te 3d spectrum for ZnTe/CoTe$_2$@NC in Figure 2e are attributed to the Te 3d$_{5/2}$ and Te 3d$_{3/2}$ orbitals of Te^{2-}, whilst the peaks at 576.5 and 586.7 eV most likely result from tellurium oxide on the surface of tellurides.[15] A negative shift of binding energy is readily observed in Te 3d$_{5/2}$ and Te 3d$_{3/2}$ from CoTe$_2$@NC to ZnTe/CoTe$_2$@NC. This finding confirms excess electrons around Te in ZnTe/CoTe$_2$@NC heterostructure, which will act as a negative charge center to attract cations and promote fast ionic diffusion kinetics in PIBs.[26] Additionally, three types of nitrogen species can be readily identified in ZnTe/CoTe$_2$@NC following deconvolution of the high-resolution N 1s XPS spectra in which pyridinic-type nitrogen takes a significantly greater ratio (Figure S10 and Table S1, Supporting Information). These observations combined, confirm the formation of the ZnTe/CoTe$_2$@NC heterostructure via the introduction of Zn species within Co-ZIF-67.

Electrochemical performance evaluation of the as-synthesized ZnTe@NC, CoTe$_2$@NC, ZnTe/CoTe$_2$@NC, and commercial graphite material as anode electrodes in PIBs was conducted systematically (**Figure 3**, FiguresS11–S13, Supporting Information) to determine the impact of the synthesized heterostructures on resulting electrochemical properties. Figure 3a presents the continuous cyclic voltammetry (CV) curves in a half-cell within the voltage range of 0.01–3.0 V that were determined. For ZnTe/CoTe$_2$@NC electrode, an evident cathodic peak is observed at 0.71 V in the first cycle that disappears in subsequent cycles. This finding is attributed to the formation of stable solid-electrolyte interphase (SEI) film on the surface of the electrode. The lesser peaks in the range 0.7 to 0.1 V most likely correspond to a series of conversion reactions from ZnTe/CoTe$_2$ to Zn, Co, and K$_x$Te phases, a consistent finding with separate reports.[14,27] In the anodic scan a series of peaks appear from 1.0 to 2.1 V that correspond to the multistep transformation reaction from products to ZnTe and CoTe$_2$. The CV curves exhibited comparable curve shape with near complete overlapping. This finding underscores the high reversibility of electrochemical reaction of the ZnTe/CoTe$_2$@NC electrodes. The CV profiles for ZnTe@NC and CoTe$_2$@NC are similar to those for ZnTe/CoTe$_2$@NC with only varied voltage values during scanning, indicating the same electrochemical reactions are existed (Figure S14, Supporting Information). From the findings of deconvoluted differential capacity (Figure S15, Supporting Information), CoTe$_2$ makes a significantly greater capacity contribution during cycling. Additionally, the galvanostatic charge-discharge profiles for ZnTe/CoTe$_2$@NC electrode exhibit a charge capacity of, respectively, 486.1, 491.4, 444.1, and 440.3 mAh g^{-1}
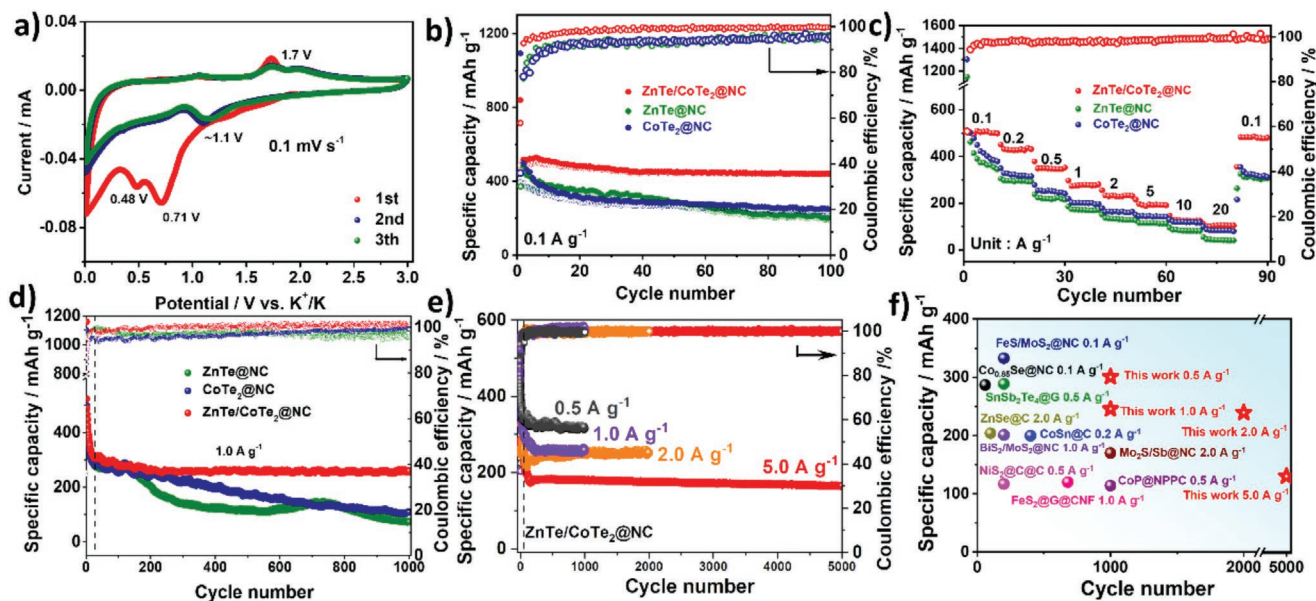
Figure 3. Electrochemical performance for as-synthesized ZnTe@NC, CoTe$_2$@NC, and ZnTe/CoTe$_2$@NC electrodes for K-ion storage. a) Cyclic voltammetry curves for ZnTe/CoTe$_2$@NC electrode. b) Cycling performance at 0.1 A g^{-1}. c) Rate performance. d) Long-term cycling performance at 1 A g^{-1}. e) Long-term cycling of ZnTe/CoTe$_2$@NC electrode at varying rate and corresponding Columbic efficiency. f) Comparison of selected materials for high-rate PIBs.

at 1st, 10th, 50th, and 100th cycle, with a Coulombic efficiency (CE) of ≈100% following a continuous 100 cycles (Figure 3b and Figure S16, Supporting Information). From the comparison, both ZnTe@NC with 195.9 mAh g^{-1} and CoTe$_2$@NC with 236.9 mAh g^{-1}, at the 100th cycle, are seen to exhibit significantly less performance at the identical current density (Figure S17, Supporting Information). The initial Coulombic efficiency of ZnTe/CoTe$_2$@NC is 58.3%, which is much higher than that in ZnTe@NC (30.1%) and CoTe$_2$@NC (40.0%). It is concluded that these findings confirm an outstanding electrochemical reversibility and high rate potassiation of the heterojunction. The K$^+$ ions react with ZnTe/CoTe$_2$@NC because of ready access to active components, electron-rich Te environment and the built-in electric field.

The rate capability of all as-synthesized new structures is summarily presented in Figure 3c. It is seen from the figure that when the current density increases from 0.1 to 20.0 A g^{-1}, the ZnTe/CoTe$_2$@NC electrode exhibits the highly significant reversible capacity of, respectively, 498.7, 430.8, 352.1, 279.9, 233.3, and 190.2 mA h g^{-1} at 0.1, 0.2, 0.5, 1.0, 2.0, and 5.0 A g^{-1}, that when the current density falls to 0.1 A g^{-1} there is a recovered capacity of 480.3 mA h g^{-1}. The ZnTe/CoTe$_2$@NC heterostructures reveal a good stability with a capacity of 257.9 mAh g^{-1} after 1000 cycles at 1 A g^{-1} (Figure 3d). It is concluded from these results therefore that a ZnTe/CoTe$_2$@NC electrode outperforms in capacity reversibility and stability, all single-phase materials, as shown in (Figure 3c,d and Figure S17c, Supporting Information).

Figure 3e presents a comparative summary of the high-rate performance of the electrodes determined from long-term cycling performance at varying current density. As is seen in the figure, after initial activation process, the ZnTe/CoTe$_2$@NC exhibits a significantly more stable ultra-long cycling performance

when compared with that in ZnTe@NC and CoTe$_2$@NC electrodes. Following a continuous 1000 cycles, respectively, 317.5 and 261.3 mA h g^{-1} were retained for ZnTe/CoTe$_2$@NC at a current density 0.5 and 1.0 A g^{-1}. This finding evidences its highly significant long-term cycling stability. The fading rate of specific capacity at 1.0 A g^{-1} is just 0.016% (from 30th to the 1000th cycle) when compared with that in ZnTe@NC and CoTe$_2$@NC counterparts, which indicates the outstanding rate capability (Table S2, Supporting Information). Following 2000 cycles the specific capacity was 254.5 mA h g^{-1} at a current density of 2.0 A g^{-1}. Despite a continuous 5000 cycles the ZnTe/CoTe$_2$@NC maintained a significant reversible capacity of 165.2 mA h g^{-1} at a current density of 5.0 A g^{-1}. Although direct cycling of the electrode at high current density resulted in lower CE in the early stages, that following stabilized at >99.8% with negligible capacity fading. It is hypothesized that the highly significant electrochemical performance exhibited by ZnTe/CoTe$_2$@NC is because of synergy between enriched K$^+$ absorption sites and rapid electronic/ionic charge diffusion kinetics. To highlight the high-rate performance of the ZnTe/CoTe$_2$@NC heterostructure electrode, it was compared with reported transition-metal-dichalcogenides-based anode materials for PIBs, which outperformed all the selected anodes working at high current densities and long cycles (Figure 3f).

To assess the practical application of the new material, the ZnTe/CoTe$_2$@NC electrode was tested with lean electrolyte (20 µL) (results are presented in Figure S18, Supporting Information). In galvanostatic discharge and charge, ZnTe/CoTe$_2$@NC exhibited a capacity of 359.7 mAh g^{-1} at a current density of 0.1 A g^{-1}, and importantly, at a current density of 1.0 A g^{-1} it exhibited 212.3 mAh g^{-1} over 500 cycles together with a fading rate of 0.067% (based on 30th capacity). Because of the importance
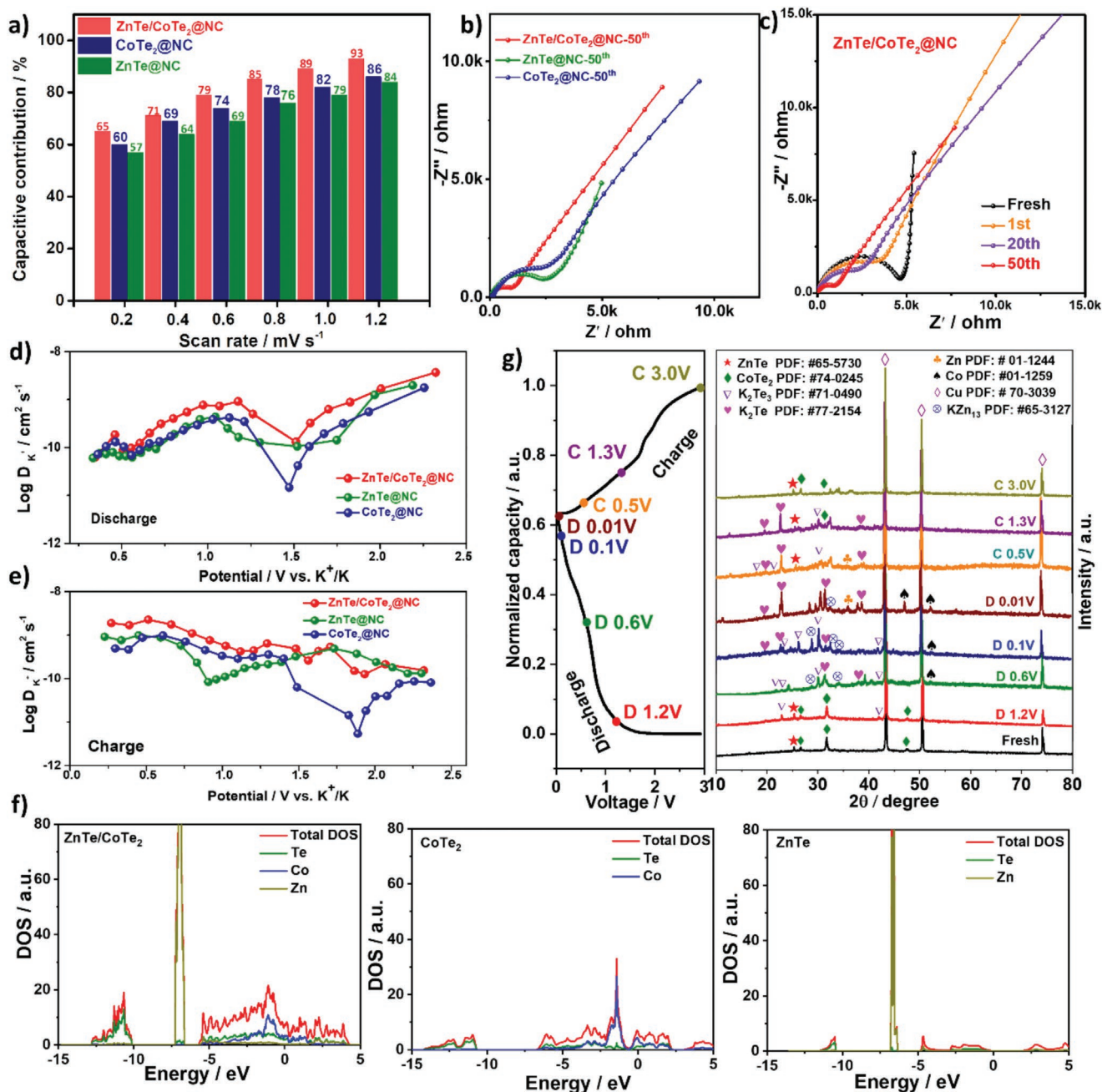
Figure 4. Electrochemical kinetic analysis for potassium storage behavior. a) Normalized contribution ratio of capacitive capacity at differing scan rate. Data are based on the CV curves. b) EIS diagram for ZnTe/CoTe₂@NC, ZnTe@NC, and CoTe₂@NC following cycling. c) EIS diagram for ZnTe/CoTe₂@NC before and following cycling. d,e) K⁺-ion diffusion coefficient computed from GITT potential profiles as a function of, respectively, depth of discharge (DOD) and state of charge (SOC). f) Theoretical computation for total density of states (TDOS) for ZnTe/CoTe₂, ZnTe and CoTe₂. g) Ex situ XRD pattern for ZnTe/CoTe₂@NC electrode at differing discharge/charge.

of electrolyte to electrochemical performance, it is anticipated that the performance of the ZnTe/CoTe₂@NC heterostructure will be boosted by its optimization.[6,28] These results highlight ZnTe/CoTe₂@NC as a potential anode for practical PIBs for high-rate application.

To gain insight into the mechanism of rate performance of the ZnTe/CoTe₂@NC anode for PIBs, selected quantitative analyses were carried out as summarized in **Figure 4**. Experimental

results strongly evidence a surface capacitance-dominated process in electrodes of ZnTe/CoTe₂@NC, based on findings from the CV curves at different scan rates, together with the relationship between measured anodic peak current density and the sweep rate (Figure S19, Supporting Information). The ratio of the capacitive contribution of all three telluride anodes to current at a fixed voltage is determined by the separation of the current i into diffusion-controlled, and capacitive,

**ADVANCED
SCIENCE NEWS**

www.advancedsciencenews.com

**ADVANCED
ENERGY
MATERIALS**

www.advenergymat.de

contributions at the corresponding voltage. A dominant capacitive contribution of ≈85% is seen at a scan rate of $0.8\,mV\,s^{-1}$ for $ZnTe/CoTe_2@NC$ electrode, however, with increasing scan rate the capacitive contribution increases, and a maximum capacitive contribution of 93% is exhibited at the scan rate $1.2\,mV\,s^{-1}$, as is shown in Figure 4a. In contrast, the visible decrease in the capacitive contribution under identical scan rates from $ZnTe/CoTe_2@NC$ to $ZnTe@NC$ and $CoTe_2@NC$ arises, dominantly, from less accessible active sites, or electronic/ionic diffusion limitation.[29] In addition, the electrochemical impedance spectroscopy (EIS) diagram for $ZnTe/CoTe_2@NC$ following 50 cycles (Figure 4b) shows one-semicircle followed by a low-frequency Warburg component that is highly indicative of diffusion through a semi-infinite medium.[30] $ZnTe/CoTe_2@NC$ exhibited a significantly lower value of R_{ct} (charge transfer resistance) of $1012.0\,\Omega$ compared with $2890.2\,\Omega$ for $ZnTe@NC$ and $2471.7\,\Omega$ for $CoTe_2@NC$ (Figure S20 and Table S3, Supporting Information). This significantly lower charge-transfer resistance for $ZnTe/CoTe_2@NC$ confirms the improved electronic conductivity and facilitated K^+-ion diffusion as a direct result of the unique heterostructure.[31,32] The EIS diagram for $ZnTe/CoTe_2@NC$ electrode prior and following cycling (Table S3, Supporting Information) underscores a highly significant change in impedance, which is reasonably attributed to a more compatible interface between electrode and electrolyte following numerous cycles.[33]

To assess any correlation between electrochemical properties and structure of $ZnTe/CoTe_2@NC$ electrode for PIBs, galvanostatic intermittent titration technique (GITT) measurement and theoretical computation were determined as summarized in Figure 4d–f. The voltage responses for $ZnTe/CoTe_2@NC$, $ZnTe@NC$ and $CoTe_2@NC$ electrodes in the third cycle showed $ZnTe/CoTe_2@NC$ exhibited least overpotential (Figure S21a, Supporting Information). The ionic diffusion coefficients for $ZnTe/CoTe_2@NC$ ($10^{-9} - 10^{-10}$) computed from GITT curves are greater than those for $ZnTe@NC$ and $CoTe_2@NC$ in both K^+ ion insertion, and K^+ ion extraction, Figure 4d–e. The greater value of the diffusion coefficients for $ZnTe/CoTe_2@NC$ electrode means practically a boosted high-rate performance compared with the single-phase counterparts (Figure 3c). From the theoretical computations (Figure 4f and Figure S22, Supporting Information) for both $ZnTe$ and $CoTe_2$, the total density of states (TDOS) highlighted bandgaps that are not continuous at the Fermi level and confirm a semiconducting nature.[34] In contrast, the conduction band for $ZnTe/CoTe_2$ contained a significant hybridization band that gives rise to a significantly greater TDOS for $ZnTe/CoTe_2$ compared with those for $ZnTe$ and $CoTe_2$ at the Fermi level, which indicates a significantly boosted electronic conductivity in $ZnTe/CoTe_2$.

To determine the phase transformation mechanism of $ZnTe/CoTe_2@NC$ electrode during initial potassiation/depotassiation ex situ XRD and ex situ XAS (X-ray absorption spectroscopy) analysis in differing discharge and charge states were obtained, as is summarized in Figure 4g. The XRD pattern for the fresh electrode confirmed the crystallinity of the as-synthesized $ZnTe/CoTe_2@NC$ phase. Findings were that for the initial discharge several initial $ZnTe/CoTe_2@NC$ peaks

disappeared gradually and newly generated K_2Te_3, KZn_{13}, and Co peaks emerged at ≈0.6 V. With discharge to 0.01 V, the XRD patterns highlighted that all diffraction peaks related to $ZnTe/CoTe_2@NC$ had almost vanished, and peaks appeared that were almost certainly associated with metallic species Zn and Co, K_2Te and alloy KZn_{13}, which underscored continued conversion and emerging alloy reactions. When the electrode was charged to 1.3 V, K_2Te_3 appeared, and $ZnTe/CoTe_2@NC$ material remained detected. Following charging the electrode to 3.0 V, the representative peaks for $ZnTe/CoTe_2@NC$ are partially recovered. This result highlights an intensive reduction in grain-size of metallic-telluride particles with low crystallinity, or possible amorphization of $ZnTe/CoTe_2$.[32] Importantly, this is in agreement with findings from the in situ synchrotron powder XRD pattern (Figure S23, Supporting Information) and ex situ XAS analysis (Figure S24, Supporting Information).

To visualize the evolution of the hetero-interface following cycling, ex situ SEM and HRTEM analyses were determined for $ZnTe/CoTe_2@NC$, $ZnTe@NC$, and $CoTe_2@NC$ in the after terminal-potassiation to 0.01 V and after terminal-depotassiation to 3.0 V at cycle 50 at 0.1 A g^{-1}, **Figure 5** (Figure S25–S30, Supporting Information). As is seen in the figure following discharge to 0.01 V after 50 cycles, the heterostructure in $ZnTe/CoTe_2@NC$ was preserved with a uniform, thin and robust SEI layer-coating on the outer surfaces of the carbon networks, protecting $ZnTe/CoTe_2@NC$ electrode from huge structural fracturing. Importantly the ZnTe and $CoTe_2$ nanoparticles maintained pristine morphology without any significant particle aggregation, as clear demonstrated in Figure 5b–c and Figure S25, Supporting Information). This uniformity is further evidenced in the EDS mapping images (Figure 5d). In the full-depotassiation state (Figure 5e–h and Figure S26, Supporting Information) there was no apparent structural degradation. This finding highlights high-level reversibility of the $ZnTe/CoTe_2@NC$ material. Because of this $ZnTe/CoTe_2@NC$ heterostructure boosts high CE and results in highly significant rate cyclability during long-term cycling. The $ZnTe@NC$ and $CoTe_2@NC$ electrodes in contrast, however, exhibit significant carbon-shell pulverization and particle aggregation in all stages (Figure S27–S30, Supporting Information). It is concluded that the: i) agglomeration and/or pulverization during potassiation/de-potassiation leads to rapid structural-degradation of both $ZnTe@NC$ and $CoTe_2@NC$ anodes with capacity loss and cycling decay, a finding consistent with that for conversion-type anodes in lithium ion batteries;[31,35,36] and, ii) formation and conversion of ZnTe and $CoTe_2$ particles is achieved in a controlled manner because of the $ZnTe/CoTe_2@NC$ heterostructure in which particle aggregation is minimized during cycling (Figure 5i,j).

The practical application $ZnTe/CoTe_2@NC$ as an anode in PIBs was further assessed in a full-cell (Figure S31, Supporting Information). When coupled with a Potassium Prussian Blue cathode, the full-battery exhibited high cycling stability with a stable capacity of ≈110.0 mAh g^{-1} over 100 continuous cycles, Figure 5k. This performance is likely to improve when high voltage cathode materials are used underscoring the inherent advantage of $ZnTe/CoTe_2@NC$.
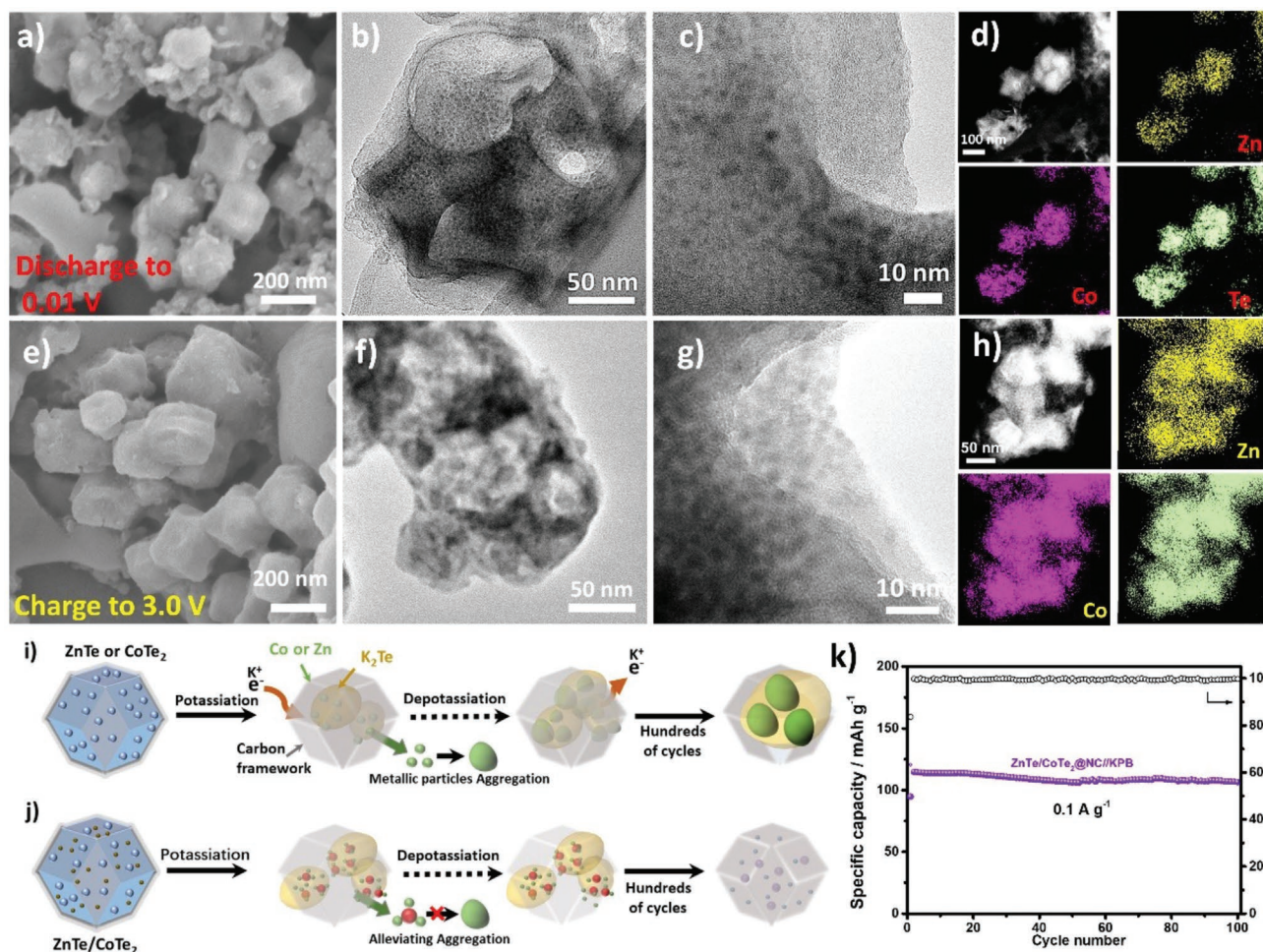
Figure 5. SEM and HRTEM image analyses for ZnTe/CoTe₂@NC electrode following 50 cycles at selected stages. Following terminal potassiation to 0.01 V: a) SEM image, b) TEM image, c) HRTEM image, and d) EDS mapping of the selected area. Following terminal de-potassiation to 3.0 V: e) SEM image, f) TEM image, g) HRTEM image, and h) EDS mapping of the selected area. i,j) Proposed mechanism for charge and discharge. k) Electrochemical performance of full cell battery.

3. Conclusion

In summary, a ZnTe/CoTe₂@NC heterostructure synthesized by a new facile method significantly boosted charge transfer kinetics in a potassium-ion battery. Combined experiment and theoretical computation confirmed that synthesis of the metallic telluride heterostructure with built-in electric fields promoted structural stability that resulted in boosted ionic and electronic diffusion kinetics with excellent high-rate capability. We conclude that the metallic tellurides heterostructure will be attractive to practically control tuning of the activity of tellurides for ready uptake of potassium ions, and, importantly, other ions with a large radius. Our findings offer a quantitative basis for design of fast and durable charge transfer in materials and will therefore be of immediate benefit for design of low-cost batteries for large-scale energy storage and conversion.

Supporting Information

Supporting Information is available from the Wiley Online Library or from the author.

Conflict of Interest

The authors declare no conflict of interest.

Data Availability Statement

The data that support the findings of this study are available from the corresponding author upon reasonable request.

[1] H. Huang, R. Xu, Y. Feng, S. Zeng, Y. Jiang, H. Wang, W. Luo, Y. Yu, *Adv. Mater.* **2020**, *32*, 1904320.

[2] W. Zhang, M. Sun, J. Yin, K. Lu, U. Schwingenschlögl, X. Qiu, H. N. Alshareef, *Adv. Energy Mater.* **2021**, *11*, 2101928.

[3] J. Ge, L. Fan, A. M. Rao, J. Zhou, B. Lu, *Nat. Sustain.* **2022**, *5*, 225.

[4] T. Hosaka, K. Kubota, A. S. Hameed, S. Komaba, *Chem. Rev.* **2020**, *120*, 6358.

[5] L. Jiang, Y. Lu, C. Zhao, L. Liu, J. Zhang, Q. Zhang, X. Shen, J. Zhao, X. Yu, H. Li, X. Huang, L. Chen, Y.-S. Hu, *Nat. Energy* **2019**, *4*, 495.

[6] Q. Zhang, Z. Wang, S. Zhang, T. Zhou, J. Mao, Z. Guo, *Electrochem. Energy Rev.* **2018**, *1*, 625.

[7] B. Lin, X. Zhu, L. Fang, X. Liu, S. Li, T. Zhai, L. Xue, Q. Guo, J. Xu, H. Xia, *Adv. Mater.* **2019**, *31*, 1900060.

[8] X. Li, J. Li, L. Ma, C. Yu, Z. Ji, L. Pan, W. Mai, *Energy & Environmental Materials* **2022**, *5*, 458.

[9] L. Fang, J. Xu, S. Sun, B. Lin, Q. Guo, D. Luo, H. Xia, *Small* **2019**, *15*, 1804806.

[10] S. Zhang, Q. Fan, Y. Liu, S. Xi, X. Liu, Z. Wu, J. Hao, W. K. Pang, T. Zhou, Z. Guo, *Adv. Mater.* **2020**, *32*, 2000380.

[11] J. Wu, Q. Zhang, S. Liu, J. Long, Z. Wu, W. Zhang, W. K. Pang, V. Sencadas, R. Song, W. Song, *Nano Energy* **2020**, *77*, 105118.

[12] Q. Peng, F. Ling, H. Yang, P. Duan, R. Xu, Q. Wang, Y. Yu, *Energy Storage Mater.* **2021**, *39*, 265.

[13] H. Zhang, Y. Cheng, J. Sun, W. Ye, C. Ke, M. Cai, H. Gao, P. Wei, Q. Zhang, M.-S. Wang, *Adv. Energy Mater.* **2022**, *12*, 2201259.

[14] X. Xu, Y. Zhang, H. Sun, J. Zhou, Z. Liu, Z. Qiu, D. Wang, C. Yang, Q. Zeng, Z. Peng, S. Guo, *Adv. Mater.* **2021**, *33*, 2100272.

[15] S. Zhang, L. Qiu, Y. Zheng, Q. Shi, T. Zhou, V. Sencadas, Y. Xu, S. Zhang, L. Zhang, C. Zhang, C.-L. Zhang, S.-H. Yu, Z. Guo, *Adv. Funct. Mater.* **2021**, *31*, 2006425.

[16] Y. Li, J. Zhang, Q. Chen, X. Xia, M. Chen, *Adv. Mater.* **2021**, *33*, 2100855.

[17] Y. Zheng, T. Zhou, C. Zhang, J. Mao, H. Liu, Z. Guo, *Angew. Chem., Int. Ed.* **2016**, *55*, 3408.

[18] G. Fang, Q. Wang, J. Zhou, Y. Lei, Z. Chen, Z. Wang, A. Pan, S. Liang, *ACS Nano* **2019**, *13*, 5635.

[19] B. Y. Xia, Y. Yan, N. Li, H. B. Wu, X. W. Lou, X. Wang, *Nat. Energy* **2016**, *1*, 15006.

[20] C. Yuan, H. B. Wu, Y. Xie, X. W. Lou, *Angew. Chem., Int. Ed.* **2014**, *53*, 1488.

[21] D. Saliba, M. Ammar, M. Rammal, M. Al-Ghoul, M. Hmadeh, *J. Am. Chem. Soc.* **2018**, *140*, 1812.

[22] S. R. Venna, J. B. Jasinski, M. A. Carreon, *J. Am. Chem. Soc.* **2010**, *132*, 18030.

[23] Y. He, L. Wang, C. Dong, C. Li, X. Ding, Y. Qian, L. Xu, *Energy Storage Mater.* **2019**, *23*, 35.

[24] X. Huang, H. Yu, H. Tan, J. Zhu, W. Zhang, C. Wang, J. Zhang, Y. Wang, Y. Lv, Z. Zeng, D. Liu, J. Ding, Q. Zhang, M. Srinivasan, P. M. Ajayan, H. H. Hng, Q. Yan, *Adv. Funct. Mater.* **2014**, *24*, 6516.

[25] P. Liu, J. Han, K. Zhu, Z. Dong, L. Jiao, *Adv. Energy Mater.* **2020**, *10*, 2000741.

[26] Y. Li, J. Qian, M. Zhang, S. Wang, Z. Wang, M. Li, Y. Bai, Q. An, H. Xu, F. Wu, L. Mai, C. Wu, *Adv. Mater.* **2020**, *32*, 2005802.

[27] J.-U. Seo, C.-M. Park, *J. Mater. Chem. A* **2014**, *2*, 20075.

[28] L. Li, Y. Zheng, S. Zhang, J. Yang, Z. Shao, Z. Guo, *Energy Environ. Sci.* **2018**, *11*, 2310.

[29] J. W. Fergus, *J. Power Sources* **2010**, *195*, 939.

[30] R.-C. Lee, J. Franklin, C. Tian, D. Nordlund, M. Doeff, R. Kostecki, *J. Power Sources* **2021**, *498*, 229885.

[31] S. Zhang, Y. Zheng, X. Huang, J. Hong, B. Cao, J. Hao, Q. Fan, T. Zhou, Z. Guo, *Adv. Energy Mater.* **2019**, *9*, 1900081.

[32] S. Zhang, J. Hong, X. Zeng, J. Hao, Y. Zheng, Q. Fan, W. K. Pang, C. Zhang, T. Zhou, Z. Guo, *Adv. Funct. Mater.* **2021**, *31*, 2101676.

[33] Q. Fan, J. Jiang, S. Zhang, T. Zhou, W. K. Pang, Q. Gu, H. Liu, Z. Guo, J. Wang, *Adv. Energy Mater.* **2021**, *11*, 2100957.

[34] Y. Shi, G. Zhan, H. Li, X. Wang, X. Liu, L. Shi, K. Wei, C. Ling, Z. Li, H. Wang, C. Mao, X. Liu, L. Zhang, *Adv. Mater.* **2021**, *33*, 2100143.

[35] D.-S. Bin, X.-J. Lin, Y.-G. Sun, Y.-S. Xu, K. Zhang, A.-M. Cao, L.-J. Wan, *J. Am. Chem. Soc.* **2018**, *140*, 7127.

[36] Y. Sun, H. Wang, W. Wei, Y. Zheng, L. Tao, Y. Wang, M. Huang, J. Shi, Z.-C. Shi, D. Mitlin, *ACS Nano* **2021**, *15*, 1652.